Distinct REY sources recorded in the Doushantuo phosphorite

Fang Zhang [a,c], Haifeng Fan [a,c,*], Xiqiang Liu [a,c], Hongjie Zhang [a,c], Hanjie Wen [b,c], Yong Tang [d,c], Pengqiang Shang [e]

[a] *State Key Laboratory of Ore Deposit Geochemistry, Institute of Geochemistry, Chinese Academy of Sciences, Guiyang 550081, China*
[b] *School of Earth Sciences and Resources, Chang'an University, Xi'an 710054, China*
[c] *University of Chinese Academy of Sciences, Beijing 100049, China*
[d] *Key Laboratory of High-Pressure Study of the Earth's Interior, Institute of Geochemistry, Chinese Academy of Sciences, Guiyang 550081, China*
[e] *China Chemical Geology and Mine Bureau, Beijing 100101, China*

ARTICLE INFO

ABSTRACT

During the Ediacaran period, massive marine phosphorites were deposited worldwide, which could represent a global sink of rare earth elements and yttrium (REY) in oceans. In the Doushantuo Formation of South China, the REY source has been preliminarily constrained as the mixed sources of seawater and terrigenous matter in these phosphorites. However, the REY composition of both seawater and terrigenous endmembers is still unclear; therefore, it's difficult to identify the contributions of seawater and terrigenous sourced REY. In this work, REY and other trace elements of bulk phosphorites, in situ carbonates, and apatite grains were analyzed from a drill core (Fangmashan) of the Doushantuo Formation in South China. Combined with mineralogical observations, the REY composition of seawater and terrigenous endmembers is well-constrained. Along the investigated Fangmashan drill core, all in situ carbonates (calcites and dolomites) show a modern seawater-like REY pattern, indicating that the REY characteristics of the Doushantuo seawater could be similar to those of modern oxic seawater without significant changes. Alternatively, apatites from the lower and upper phosphorites showed distinct REY patterns. One type of apatite in the upper phosphorites showed a modern seawater-like REY pattern, indicating authigenic REE enrichment from the seawater column. However, another type of apatite in the upper phosphorites with an REE pattern that deviated from seawater showed high ΣREY ($\sim$691.16 $\pm$ 309.78) and low Y/Ho ($\sim$40.52 $\pm$ 4.05), probably reflecting mixed REY sources and/or the effects of early diagenesis. It is noted that most apatites in the lower phosphorites are obviously enriched in light REY (LREY: La - Nd) compared to heavy REY (HREY: Ho - Lu and Y), which may represent a significant contribution of the terrestrial REY source. This study reveals that the REY composition of paleo-seawater could be similar to modern seawater as early as the Neoproterozoic and supports a significant contribution to understanding the difference in the REY composition of phosphorites in geological history.

1. Introduction

Marine phosphorites generally have higher rare earth elements and yttrium (REY) concentrations relative to other sedimentary rocks (e.g., carbonates and shales) due to the REY-enriched apatites in phosphorites (Piper, 1974; Toyoda et al., 1990). It has been reported that marine phosphorites with REY enrichment (>1000 ppm) were mainly formed during the Paleozoic Era (Emsbo et al., 2015; Chen et al., 2019). Although REY-enriched phosphorites are rarely reported in the Precambrian (total REY concentrations of ~ 4.23–599.58 ppm) (Luo, 2011; Khan et al., 2012; Xin et al., 2015; Yang et al., 2019; Chen et al., 2019),

massive marine Neoproterozoic phosphorites represent globally a large scale phosphogenesis event (Pufahl and Groat, 2017), thus representing an important source of REY deposits (Emsbo et al., 2015; Khelalfa et al., 2016).

The REY in phosphorites has been widely studied by researchers, and the REY source in phosphorites may contain multiple sources derived from seawater and terrigenous matter (Xin et al., 2015; Yang et al., 2019; Baioumy and Farouk, 2022). The REY characteristic of seawater is considered to be recorded in authigenic apatite and carbonates (Wright et al., 1987). For instance, paleo-phosphorites with modern seawater-like REY patterns indicate similar REY composition of paleo-seawater

to modern seawater (Shields and Stille, 2001). Here, REY characteristics of paleo-seawater similar to modern seawater do not mean that both periods show identic conditions (e.g., oxygen levels of atmosphere or seawater). Although oxidation of the surface water may have occurred in the Ediacaran period (Li et al., 2010; Sahoo et al., 2012; Xu et al., 2022), it is not so easy to correlate the modern seawater signatures with the paleo-seawater signatures since the modern atmospheric oxygen levels and Neoproterozoic atmospheric oxygen levels were completely different (Liu et al., 2021). Therefore, the comparison of REY signatures between modern and paleo-seawater is based on the presumption that REY sources are consistent, and it is speculated that REY of paleo-seawater experienced a differentiation process similar to that of the modern marine environment according to the same REY distribution patterns. Some researchers also argued that the paleo-seawater could have a different REY composition from modern seawater (e.g., HREY enrichment) following the observation of middle REY (MREY: Sm - Dy) enrichment (such as "cap-shaped" REY patterns) in paleo-phosphorites (McArthur and Walsh, 1984; Grandjean et al., 1987; Grandjean-Lécuyer et al., 1993; Ilyin, 1998; Picard et al., 2002), although it may be caused by MREY enrichment during early/late diagenesis (Emsbo et al., 2015). Detailed studies of microbial carbonates and granular phosphorites showed that the REY composition of Phanerozoic seawater has not changed (Shields and Stille, 2001; Shields and Webb, 2004). However, the REY composition of Precambrian seawater is still unclear due to the influence of terrigenous REY (Xin et al., 2015; Francovschi et al., 2020).

The REY in seawater is derived mainly from the river input, atmospheric particle deposition, and hydrothermal activity on the seafloor (Nozaki, 2001). The source of REY in the Ediacaran phosphorites from the Nanhua Basin has been studied recently by several researchers (Xin et al., 2015; Yang et al., 2021; Yang et al., 2022). Massive phosphorites of the Ediacaran Doushantuo Formation have REY characteristics similar to seawater (e.g., negative Ce anomalies and high Y/Ho ratios, >44) (Alibo and Nozaki, 1999); thus, they are considered to be derived from seawater (Yang et al., 2021). However, low Y/Ho (<44), low εNd (t) (<−5), and high $^{87}Sr/^{86}Sr$ (>0.7090) in some parts of phosphorites also indicate terrigenous REY input (Xin et al., 2015; Yang et al., 2021). REY-rich Ediacaran phosphorites (~993–2200 ppm) have also been reported in northeastern Moldova and southwestern Ukraine, and the REY enrichment was explained by the contribution of continental basalt weathering (Francovschi et al., 2020). Although the contributions of terrigenous REY have been recognized in the Doushantuo Formation phosphorites in various regions, how did the terrigenous REY contribute to the phosphorites is not well defined. Generally, the change in

terrestrial contribution is closely related to drastic climate changes (Mi, 2010; Yang et al., 2021). Specifically, the Doushantuo phosphorites was deposited after the "Snowball Earth" event that occurred ca. 635 Ma ago (Cook and Shergold, 1984), and the influence of terrigenous matter on REY enrichment in seawater and marine phosphorites is still unclear.

In this study, the REY composition of seawater and terrigenous endmember during the Doushantuo period (from 635.2 to 551.1 Ma, Condon et al., 2005) is defined by the mineralogy and geochemical parameters of carbonates and apatite and the relative contributions of terrigenous and seawater to the REY in the Doushantuo Formation phosphorites are also estimated.

2. Geological setting

The South China Block (Fig. 1A) was formed through the assembly of the Yangtze Platform with the Cathaysia Platform during the Jinning orogeny (~1.0–0.8 Ga, Li, 1999). The Chengjiang orogeny (~780–750 Ma) led to the overall assembly of the Yangtze Platform with continuous subduction and collision (Gao et al., 2018), which formed a large area of underwater uplift, which was a favorable place for phosphate deposition (Xiong et al., 2010). After the "Snowball Earth" event (including the Sturtian and Marinoan glaciations: ~720–660 Ma and ~ 640–635 Ma, respectively, Kennedy et al., 1998; Hoffman et al., 2017), the severe perturbations to Earth's climate system promoted the ocean phosphorus cycle (Reinhard et al., 2017; Li et al., 2021), and massive phosphorites with economic significance were formed in the Nanhua Basin during the Ediacaran Doushantuo period (Tian, 2000).

Massive phosphorites of the Doushantuo Formation were widely deposited in the Yangtze Platform, which are mainly distributed in four phosphorus accumulation areas in central Guizhou, western Hunan, northern Hunan, and western Hubei (Fig. 1B, Tian, 2000). Our research is focused on the phosphorus accumulation area of western Hubei (Fig. 1B), which includes five large phosphorus ore areas: Baokang, Xinhua, Shennongjia, Yichang, and Jingxiang (Fig. 2, Xiong et al., 2010). The paleogeographic location of phosphate deposits in western Hubei is limited to shallow water areas (Liang, 1984), and the phosphorites are mainly distributed in the distal and proximal side of shelf lagoon facies and are rare in the shelf margin facing the open ocean (Fig. 2) (Jiang et al., 2011; Zhu et al., 2013). The sedimentary sequences from the study area were accumulated in an inner shelf depositional environment (Fig. 1B) (Vernhet, 2007; Jiang et al., 2011).

The Doushantuo Formation in western Hubei has four phosphate members in the Jingxiang phosphate deposit area, both the first and
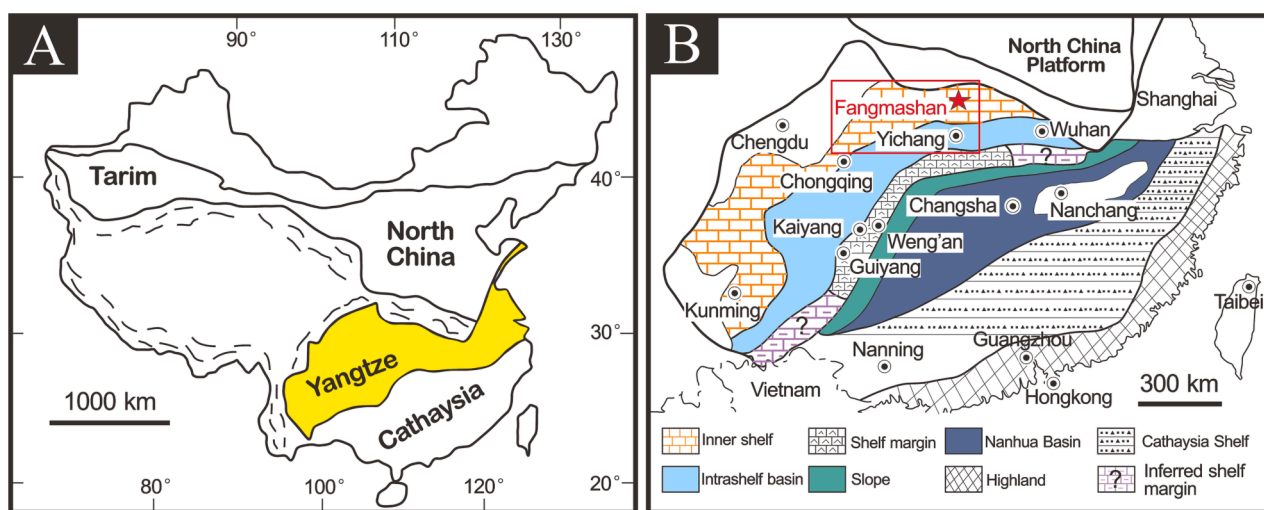

Fig. 1. (A) Generalized geological map of China. (B) The sedimentary facies in the Yangtze Platform during the Ediacaran period (modified after Jiang et al., 2011). The red rectangle and red star indicate the position of western Hubei province and the studied drill core. (For interpretation of the references to colour in this figure legend, the reader is referred to the web version of this article.)
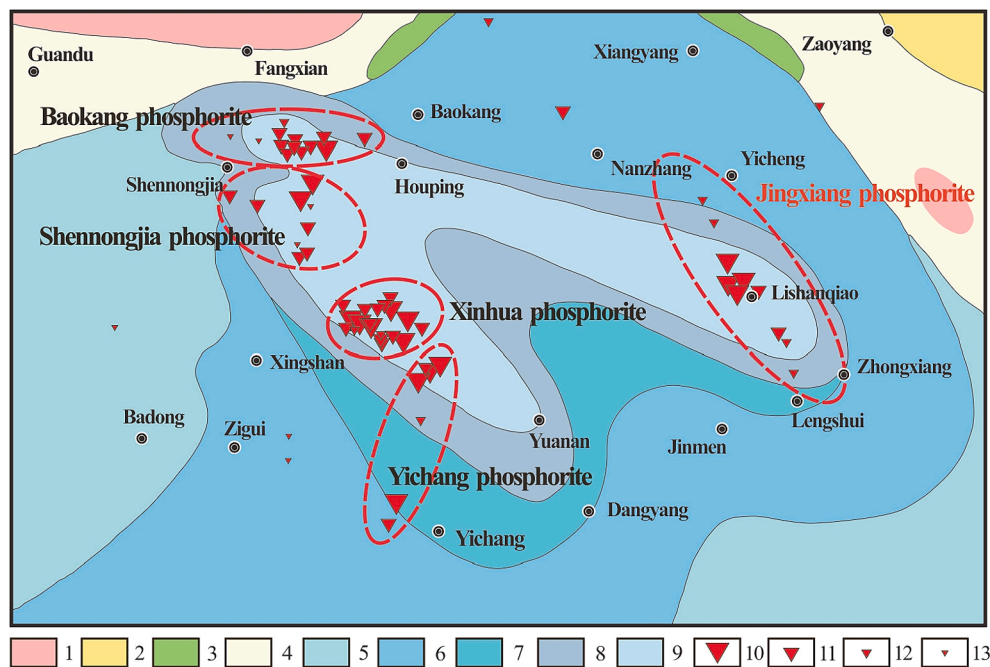
Fig. 2. The lithofacies paleogeographic map during Doushantuo period in the ore concentrated district of the western Hubei province (modified after Xiong et al., 2010). Legend: 1. Ancient land and island; 2. Littoral volcanic facies; 3. Littoral tidal flat-sandstone or siltstone, sandy rock, and carbonate subfacies; 4. Littoral tidal flat-carbonate sandstone and mudstone subfacies; 5. Coastal basin-carbonate and mudstone subfacies; 6. Coastal basin-mudstone and carbonate subfacies; 7. Coastal basin margin-phosphate mudstone and carbonate subfacies; 8. Coastal platform slope-phosphate rock, mudstone and dolostone facies; 9. Coastal platform-phosphorite, mudstone, and carbonate subfacies; 10. Large-sized phosphorite; 11. Medium-sized phosphorite; 12. Small-sized phosphorite; 13. Phosphorite mineralization spot.

third members are economically viable (Xiong et al., 2010; Luo, 2011). The Fangmashan ore Block (~92 million tons, P_2O_5 grade of ore of ~ 21 wt%) (Liu, 2012), is selected for research (Fig. 1B, Fig. 3A). The Block has two phosphate members, correlated with the first and third members in the Jingxiang phosphate deposit area, and three wall rock members (Fig. 3B). The lower wall rocks (WR-I Member) are of siliciclastic composition and consists of siliceous shales and siliceous dolostones. WR-I Member is overlain by the lower phosphorites (LP Member) that is characterized by an alternation between phosphorites and siliceous shales or siliceous dolostones. The middle wall rocks contain thick gray dolostones (WR-II Member) and gray or dark-gray silty shales or mudstones (WR-III-a Member). The upper phosphorites (UP Member) mainly occur as a massive structure but are also represented by banded phosphorites interbedded with thin dolostones. The upper wall rocks (WR-III-b Member) show the same lithological and geochemical characteristics as WR-III-a Member, so it is convenient to uniformly describe them and name them with WR-III Member. Ore composition is mainly collophane and microcrystalline apatite, and the gangue mineral predominantly consists of dolomite, quartz, clay mineral, and pyrite.

3. Sampling and methodology

Fifty-seven samples were taken from a drill core Zk11811 from Fangmashan of Huji phosphorites in Xiaojialing, Lishan village, Shuanghe town (Fig. 1B, 31°24′48.75″ N and 112°16′50.43″ E). All samples were powdered into 200 mesh for whole-rock major and trace element analysis. Ten samples were cut to make approximately 80 μm thick sections for mineralogy and in situ geochemical analysis.

3.1. Petrography and mineralogy

Micromorphology observation and mineral distribution image shooting were performed under an optical microscope and a JSM-7800F scanning electron microscope at the State Key Laboratory of the Institute of Geochemistry, Chinese Academy of Sciences (IGCAS). The beam current of the electric gun was 10nA, the accelerating voltage was 10–30 kV, and a focused high-energy electric beam (~1 μm) was used to bombard the mineral surface to stimulate the characteristic X-ray. The characteristic X-ray was captured by an EDAX TEAM Apollo XL energy

dispersive spectrometer to determine the chemical composition of minerals.

3.2. Major and trace elements

Major and trace element analysis was carried out following the ME-XRF26F and ME-MS61r methods, respectively, at ALS Chemex (Guangzhou) Co., Ltd. Dried powder samples were fully mixed with $Li_2B_4O_7$-$LiBO_2$-$LiNO_3$ mixed solvent, and the major elements were determined by X-ray fluorescence. The detection limit for all major elements was ~ 0.01 wt%, and the relative error and relative deviation were better than ~ 5%. Powder samples were completely digested using $HClO_4$, HNO_3, HF, and HCl and then dissolved in dilute HNO_3 (2 %) for ICP-MS measurement. A quantitative Rh internal standard solution was added to correct the matrix effect and instrument drift. The detection limits of trace elements are as follows: Ce, Ho, Lu, Tb, and Tm (~0.01 ppm); Er, Eu, Pr, Sm, and Yb (~0.03 ppm); Dy and Gd (~0.05 ppm); Y and Nd (~0.1 ppm); Sr and Th (~0.2 ppm); La and Zr (~0.5 ppm). The relative error and relative deviation were < 10%.

3.3. In situ trace elemental analysis

In situ trace element concentrations of apatite, calcite, and dolomite were analyzed by LA-ICP-MS (Agilent 7900 ICP-MS equipped with a GeolasPro 193-nm ArF excimer laser) at the State Key Laboratory of the IGCAS. The beam size of all minerals was ~ 44 μm, the laser pulse energy was 65 mJ, and the pulse frequency was 10 Hz. Each analysis consisted of 30 s of blank (laser-off) and 50 s of sample ablated signals. Element abundance of all minerals was calibrated using the NIST610 and NIST612 standards, and Durango and MACS-3 standards were used as apatite and carbonate external standards, respectively. Data calculation was processed with ICPMSDataCal software (Liu et al., 2008). Elemental analysis of all samples was applied by internal standard-independent calibration, with calcium as the standard internal element.

3.4. Element calculation

The REY concentration was normalized to Post-Archean Australian shales (Taylor and McLennan, 1985). Ce anomaly (Ce/Ce*) was
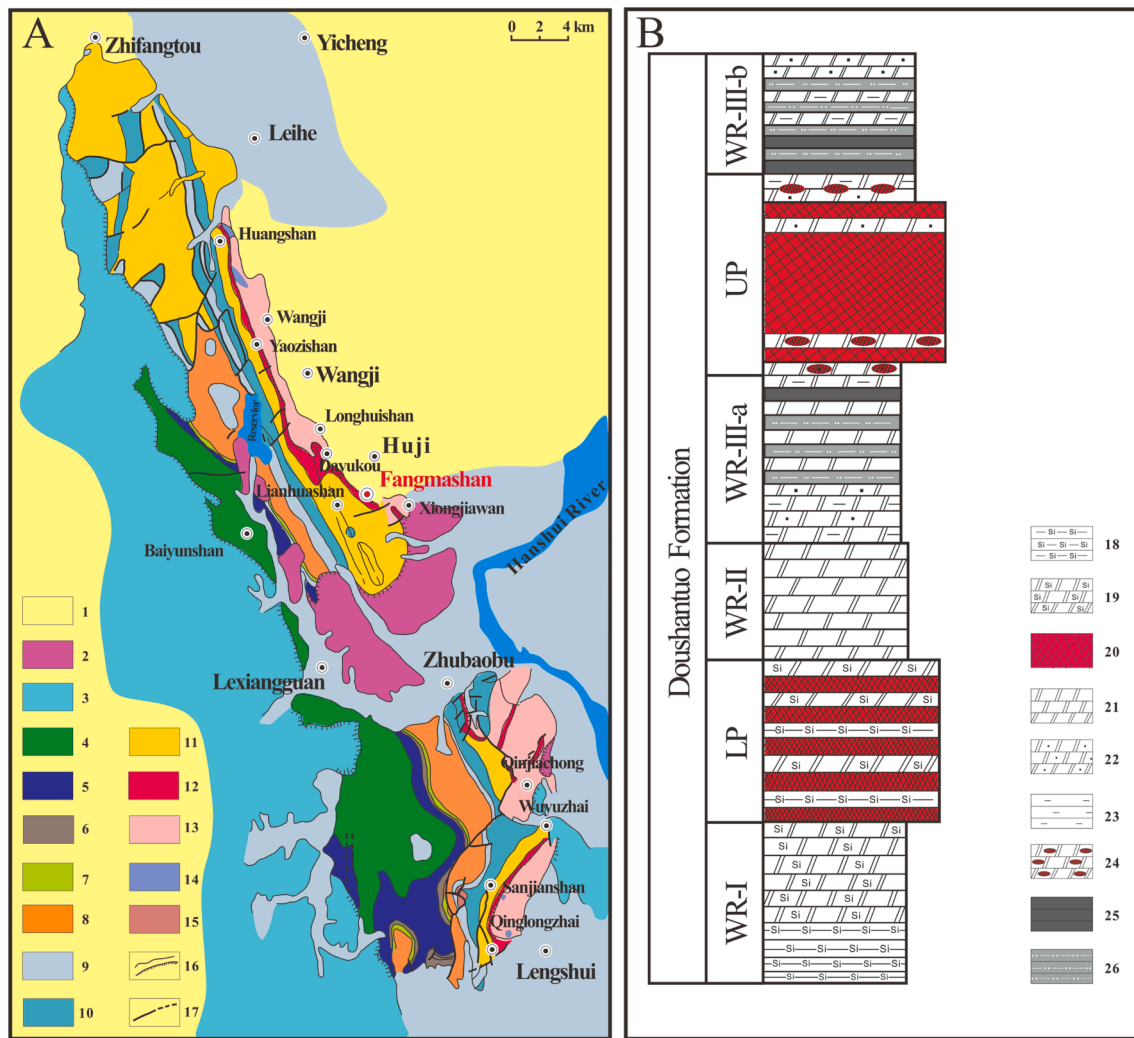
Fig. 3. (A). Regional geological map of Jingxiang phosphorite (modified after Luo, 2011). (B). Simplified stratigraphic column of the Fangmashan borehole near the Huji village. Legend for A and B: 1. Quaternary; 2. Cenozoic; 3. Cretaceous; 4. Triassic; 5. Permian; 6. Carboniferous; 7. Devonian; 8. Silurian; 9. Ordovician; 10. Cambrian; 11. Ediacaran Dengying Formation; 12. Ediacaran Doushantuo Formation; 13. Mesoproterozoic (granitic gneiss and chlorite schist); 14. Yanshanian (199.6–133.9 Ma) granites; 15. Jinningian (1.0–0.8 Ga) granites; 16. The geological boundary of conformity and unconformity; 17. Measured fault and inferred fault; 18. Siliceous shale; 19. Siliceous dolostone; 20. Phosphorite; 21. Dolostone; 22. Silty dolostone; 23. Muddy dolostone; 24. Phosphatized dolostone; 25. Black shale; 26. Dark or dark-grey silty shale or mudstone.

calculated using the conventional calculation formula: $Ce/Ce* = 2 \bullet Ce_N/(La_N + Pr_N)$ (Bau and Dulski, 1996). The bell shape index (BSI) value was used to detect the enrichment degree of MREY: $BSI = ((2 \bullet (Sm_N + Gd_N + Dy_N)_{average})/((La_N + Pr_N + Nd_N)_{average} + (Ho_N + Er_N + Tm_N + Yb_N + Lu_N)_{average}))$ (Taylor and McLennan, 1985).

4. Result

4.1. Mineralogy

4.1.1. Wall rocks

The predominant minerals of WR-I Member are K-feldspar and calcite, which usually exist in the form of cement. Abundant pyrite grains with particle sizes varying from several microns to hundreds of microns were observed in WR-I Member, and their particle size can reach 200 μm. Calcite and dolomite were the most common mineral constituents of the WR-II Member, with insignificant amounts of clastic material. The main mineralogical species in WR-III Member were dolomite, quartz, and K-feldspar, which usually exist in the form of cement. Apatite is identified only in the WR-III Member, shows an irregular shape, and is mainly cemented by quartz and dolomite

(Fig. 4A). The particle size of apatite is up to ~ 200 μm, and the smaller-sized pyrite grains (<100 μm) are in close contact with it.

4.1.2. UP Member

In the UP Member, apatite, quartz, pyrite, dolomite, and calcite are the main minerals (Fig. 4B). Apatite is closely associated with quartz and in a blocky shape without obvious boundary (Fig. 4B) and present either as well-crystallized (Fig. 4C) or structureless aggregates as collophane (Fig. 4D). There are also 100–300 μm apatite grains, often wrapped with long and irregular calcite grains (Fig. 4B). Pyrite grains are small, most of which are only a few microns in size and are scattered. In addition, hexagonal pyrite grains (not shown) of particle size 50–80 μm are observed with good euhedral crystals.

4.1.3. LP Member

Apatites in the LP Member are interbedded with a clastic layer comprising feldspar and quartz (Fig. 4E) or a mineral layer comprising quartz and calcite (Fig. 4F). Apatite is mainly stacked in layers and has smooth and flat edges (Fig. 4G), and another type of apatite shows fuzzy crystals and characterized by collophane (Fig. 4H). Pyrite grains are widely distributed with a particle size of hundreds of microns. Moreover,
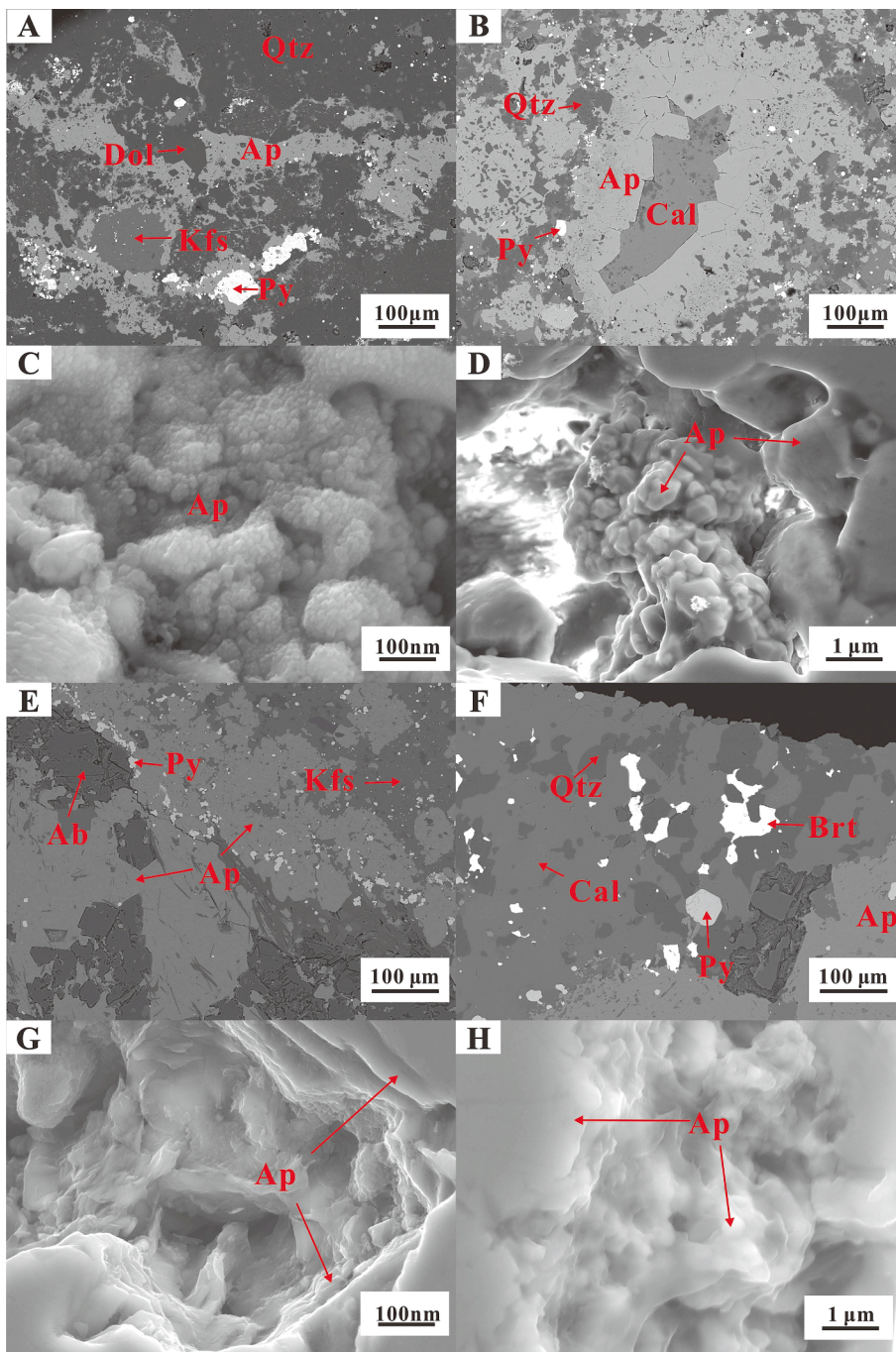
Fig. 4. Textural characteristics of the apatite, dolomite, calcite, pyrite, and barite from the analysed Ediacaran drill core samples. A and B, the scanning electron microscope (SEM) images of mineral correlation in the upper wall rock and the upper phosphorite; C and D, the secondary electron images of apatite in the upper wall rock and the upper phosphorite. E and F, scanning electron microscope (SEM) images of mineral correlation in the lower phosphorite. G and H, secondary electron images of apatite in the lower phosphorites. Abbrrrreviations: Ap = apatite, Dol = dolomite, Cal = calcite, Py = pyrite, Qtz = quartz, Brt = barite, Ab = Albite, Kfs = K-feldspar.

a large number of barite grains are observed, which are often closely associated with calcite and quartz or cemented by them.

4.2. Major and trace elements

Supplementary Data Table S1 lists the results of the major and trace element analyses. WR-I Member (mean ~ 0.79%), WR-II Member (mean ~ 0.48%), and WR-III Member (mean ~ 0.68%) have low P_2O_5 contents. Both WR-I Member (mean ~ 4.02%) and WR-III Member (mean ~ 1.09%) have higher Al contents than WR-II Member (mean ~ 0.16%). WR-I Member shows two types of REY patterns: the right-leaning REY pattern (La_N/Yb_N: ~1.16–4.80, Gd_N/Yb_N: ~0.92–3.30, Fig. 5A) and the left-leaning pattern (La_N/Yb_N: ~0.22–0.64, Gd_N/Yb_N: ~0.32–1.02, Fig. 5A). WR-II Member has a left-leaning pattern (mean La_N/Yb_N and

Gd_N/Yb_N values of ~ 0.43 and ~ 0.86, Fig. 5B), and WR-III Member has an MREY-enriched pattern (mean La_N/Yb_N, Gd_N/Yb_N and BSI values of ~ 0.71, ~1.45 and ~ 1.24, respectively, Fig. 5C). WR-I Member has a higher ΣREY content (mean ~ 165.63 ppm) than WR-III Member (mean ~ 35.95 ppm), and WR-II Member has the lowest ΣREY content (mean ~ 7.48 ppm). The ΣREY and P_2O_5 contents show a positive correlation (R^2 = ~0.59) in WR-III Member, but show no correlation in WR-I Member and WR-II Member (Fig. 6A). Moreover, the ΣREY and Al contents have a clear positive correlation in WR-I Member (R^2 = ~0.52), WR-II Member (R^2 = ~0.84) and WR-III Member (R^2 = ~0.78) (Fig. 6B). It is worth noting that only WR-I Member has no negative Ce/Ce* (mean ~ 1), but WR-II Member (mean ~ 0.78) and WR-III Member (mean ~ 0.81) have middle negative Ce/Ce*. All wall rocks have relatively low Y/ Ho values (means of ~ 30.62, ~33.79, and ~ 33.03 for WR-I Member,
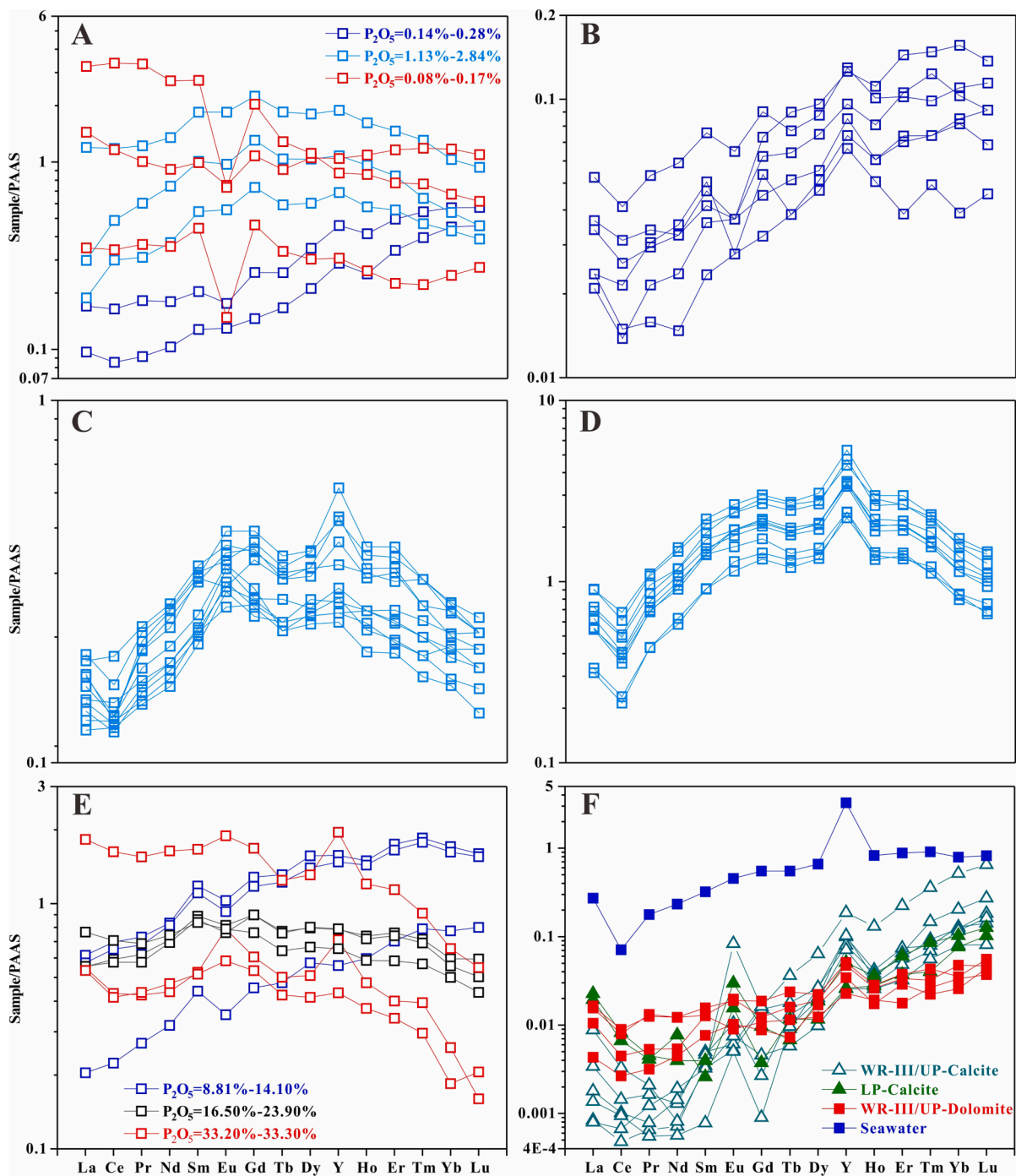
Fig. 5. A, B and C, PAAS-normalized REY patterns of the lower wall rock (WR-I), the carbonate rock interlayer (WR-II), and the upper wall rock (WR-III), respectively. D and E, the PAAS-normalized REY patterns of the upper phosphorite (UP) and the lower phosphorite (LP). F, the PAAS-normalized REY patterns of in situ carbonate minerals in WR-III, UP, and LP compared with modern seawater (Alibo and Nozaki, 1999).

WR-II Member, and WR-III Member, respectively) compared to modern oxic seawater (>44) (Alibo and Nozaki, 1999).

The UP Member contains the same P_2O_5 content (~22.34% ± 6.99%) as LP Member (~22.49% ± 10.03%) but has a lower Al content (mean ~ 0.32%) than LP Member (mean ~ 3.05%). The UP Member shows a slight MREY-enrichment pattern (mean BSI values of ~ 1.40, Fig. 5D), but the LP Member shows three types of REY pattern, including the left-leaning, the right-leaning, and the flat REY pattern (Fig. 5E). The UP Member has higher ΣREY content (~240.01 ± 70.54 ppm) than LP Member (~158.08 ± 71.83 ppm). However, the good correlation between ΣREY content and P_2O_5 content only exists in the UP Member

(Fig. 6C), all of them have no correlation between ΣREY content and Al content (Fig. 6D). The UP Member (~46.45 ± 2.73) has a significantly higher Y/Ho value than the LP Member (~32.07 ± 5.05). The LP Member has no obvious Ce/Ce* (~0.95 ± 0.08), while the UP Member shows negative Ce/Ce* (~0.61 ± 0.03).

4.3. In situ elemental analysis

Supplementary Data Table S2 and Table S3 list the in situ trace element results for apatite, calcite, and dolomite. According to the REY pattern, the apatite in the UP Member (UAp) can be divided into two
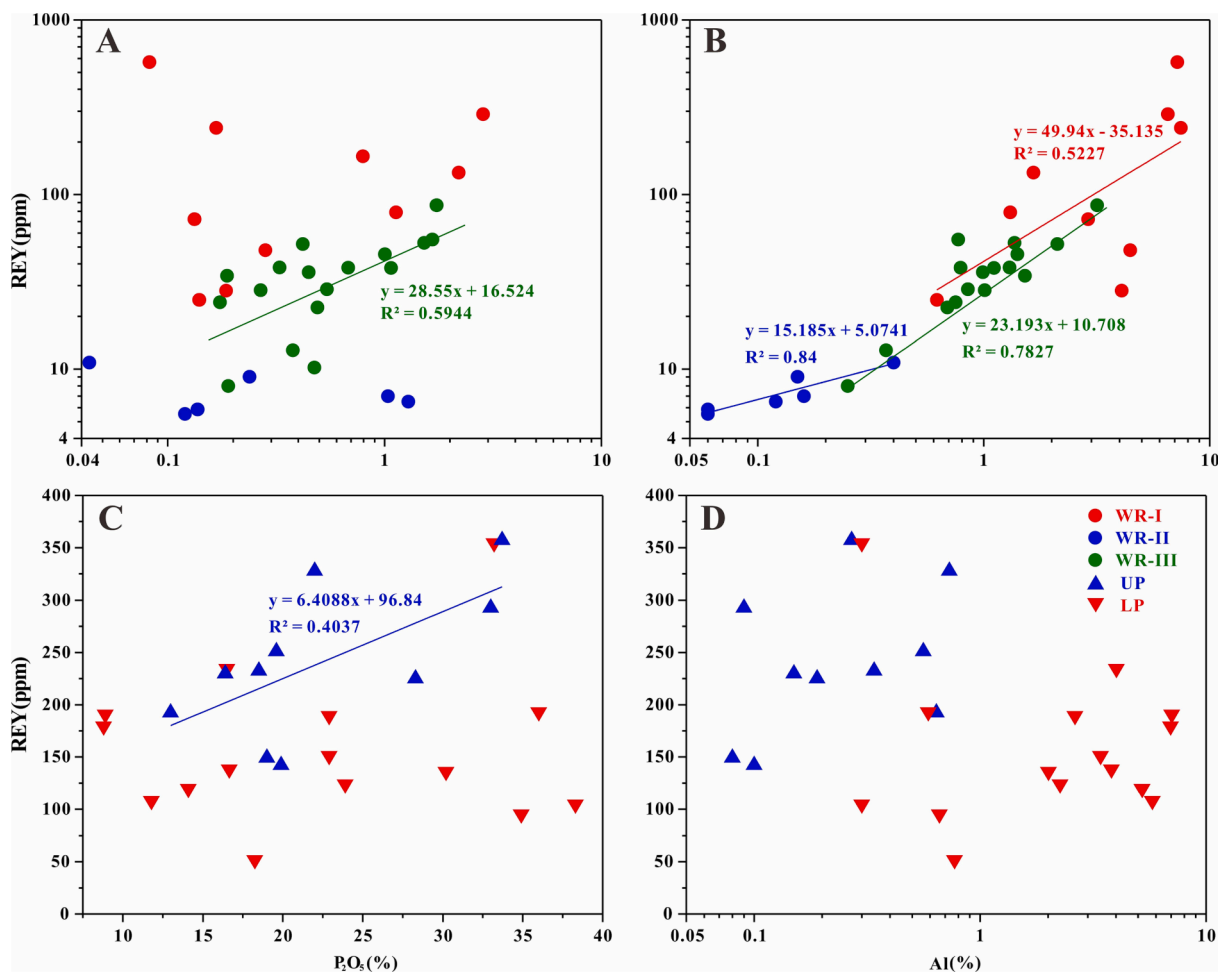
Fig. 6. A and B, the correlation between ΣREY of P_2O_5 and Al_2O_3 of the lower wall rock (WR-I), the middle wall rock (WR-II), and the upper wall rock (WR-III). C and D, the correlation among ΣREY of P_2O_5 and Al_2O_3 of the upper phosphorite (UP) and the lower phosphorite (LP).

types of apatites, UAp-I with a modern seawater-like REY pattern (mean La_N/Yb_N, Gd_N/Yb_N and BSI values of ~ 0.20, ~0.86 and ~ 1.15, respectively, Fig. 7A) and UAp-II with an MREY-enriched pattern (mean La_N/Yb_N, Gd_N/Yb_N and BSI values of ~ 0.59, ~1.88 and 1.57 respectively, Fig. 7A). The ΣREY content of UAp-II (~691.16 ± 309.78 ppm) is much higher than that of UAp-I (~132.30 ± 49.63 ppm). The apatite in

the LP Member (LAp) can also be subdivided into two types of apatites based on the REY patterns, namely, LAp-I with a right-leaning REY pattern (mean La_N/Yb_N, Gd_N/Yb_N, and BSI values of ~ 2.97, ~2.63 and 1.27, respectively, Fig. 7B) and LAp-II with a relatively flat REY pattern (mean La_N/Yb_N, Gd_N/Yb_N and BSI values of ~ 1.33, ~1.56 and 1.27, respectively, Fig. 7B). The LAp-II (~403.81 ± 95.93 ppm) contains
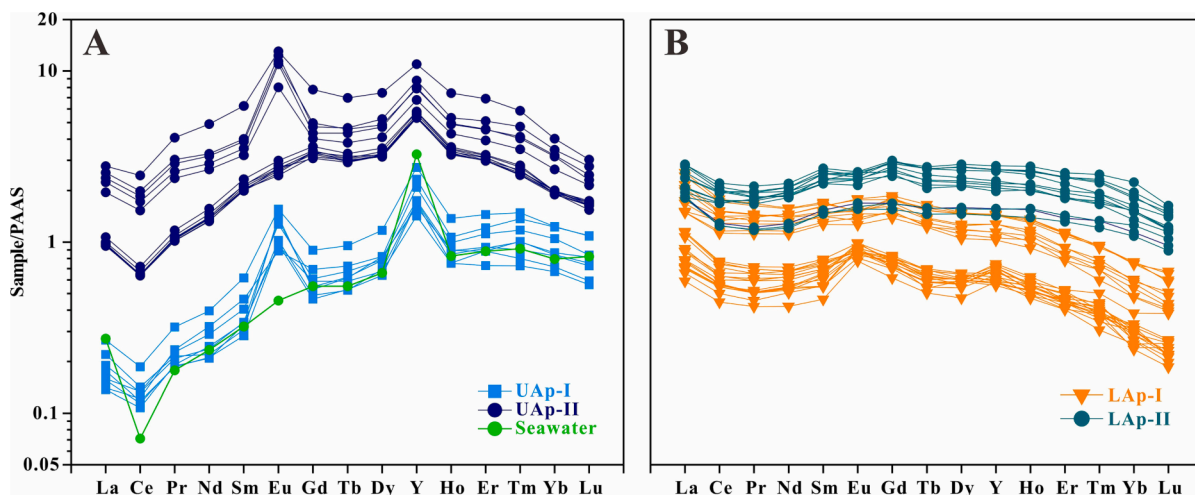

Fig. 7. PAAS-normalized REY distributions of apatites in the upper phosphorite compared with modern seawater (Alibo and Nozaki, 1999) (A) and the lower phosphorite (B).

higher ΣREY content than the LAp-I (~204.08 ± 90.71 ppm). Similar to the whole rock data, the UAp has a higher Y/Ho value (~45.65 ± 7.78) than the LAp (~30.02 ± 2.62). In addition, Y/Ho values have an obvious negative correlation with ΣREY content in the UAp (R^2 = ~0.76). The negative Ce/Ce* (~0.67 ± 0.03) is only recorded in the UAp, and the Ce/Ce* of LAp is close to ~ 1 (~0.88 ± 0.03). It is worth mentioning the higher Sr/Mn value of UAp (mean ~ 908.68) than LAp (mean ~ 35.88).

The ΣREY contents of calcite (average ~3.85 ppm) and dolomite (average ~2.82 ppm) are much lower than that of apatite. All calcite and dolomite have left-leaning patterns (mean La$_N$/Yb$_N$ and Gd$_N$/Yb$_N$ of ~ 0.32 and ~ 0.36 in dolomite, ~0.08 and ~ 0.06 in calcite, Fig. 5F), and the average LREY$_N$/HREY$_N$ are ~ 0.16 in dolomite and ~ 0.04 in calcite. It is noteworthy that part of REY (Pr - Sm) in the calcites from the LP Member (Lcal) are depleted (average La$_N$/Sm$_N$ values of ~ 5.31); this phenomenon is rare in the calcite (average La$_N$/Sm$_N$ values of ~ 0.66) of WR-III Member and the UP Member (Ucal) and dolomites (average La$_N$/Sm$_N$ values of ~ 0.91). Meanwhile, the Dy$_N$/Yb$_N$ values (mean ~ 0.15) of all calcites are coincident, and dolomites show relatively high Dy$_N$/Yb$_N$ values (mean ~ 0.5). Also, both Ucal and dolomite have high Y/Ho values (~60.76 ± 15.55 and ~ 46.16 ± 9.40, respectively) and negative Ce/Ce* (~0.33 ± 0.45 and ~ 0.46 ± 0.14, respectively). By contrast, the Lcal has low Y/Ho values (~30.75 ± 5.83) and no negative Ce/Ce* (~1.38 ± 0.53).

5. Discussion

5.1. Seawater REY during the Doushantuo period

The REY in modern oxic seawater is mainly characterized by HREY enrichment, negative Ce anomaly, and super-chondrite Y/Ho ratio (Alibo and Nozaki, 1999; Elderfield et al., 1981; Sholkovitz et al., 1994; Bau and Dulski, 1996). In the Fangmashan drill core, part of the samples in WR-I Member, WR-II Member, and LP Member have La$_N$/Yb$_N$ and Gd$_N$/Yb$_N$ ratios less than ~ 1 (Table S1), showing left-leaning REY patterns similar to modern oxic seawater (Fig. 5A, 5B, and 5E). Meanwhile, negative Ce/Ce* and high Y/Ho ratios are only recorded in WR-II Member, WR-III Member, and UP Member (Table S1, Fig. 5B, 5C, and 5D). WR-I Member and LP Member with left-leaning REY patterns have no negative Ce/Ce* and high Y/Ho values, which may be controlled by the anoxic water column or terrigenous debris input. Terrigenous-derived material usually has stable chondrite Y/Ho (~23–27) and has no negative Ce/Ce* (Nozaki et al., 1997). Thus, this may indicate that almost all samples in the Fangmashan drill core have different degrees of terrigenous debris contaminations (Y/Ho = ~26.11–49.77), where WR-I Member, LP Member, and WR-III Member (Y/Ho = ~26.11–44.37) have more terrigenous debris input than WR-II Member and UP Member (Y/Ho = ~30.91–49.77). This debris contamination can also be distinguished by typical terrestrial elements (Al, Th, Zr, etc.) (Zhao and Zheng, 2014). In Fig. 6B, the positive correlation between ΣREY content and Al$_2$O$_3$ in WR-II Member indicates that REY composition may be affected by debris. The seawater-like REY pattern of WR-II Member shows that the debris has limited impact on the REY composition of WR-II Member, or part of the WR-II Member with little terrigenous clastic input (Al$_2$O$_3$ < 0.35%) can represent the REY distribution patterns of seawater at that time (Ling et al., 2013).

LA-ICP-MS can accurately determine a single mineral, greatly avoiding the impact of terrestrial debris and significantly improving the reliability of data (Gong et al., 2021). Li et al. (2019) compared the REY compositions of the oolites of the marine carbonate rocks in the Bahamas and the seawater of the western Atlantic Ocean and found that they have similar REY distribution patterns (i.e., HREY enrichment; La, Gd, and Y positive anomaly; and Ce negative anomaly). This REY patterns similar to modern seawater has also been observed in carbonate oolites and carbonate rocks of the paleo-seawater (Shields and Webb, 2004; Zhao and Zheng, 2014; Gong et al., 2021). This is because REY in seawater can enter the mineral lattice by substituting Ca^{2+} so that the

REY characteristics of paleo-seawater can be preserved in minerals containing Ca^{2+} (Bau, 1991; Ling et al., 2013; Zhao et al., 2021). Hence, the REY characteristics of an in situ carbonate mineral can more accurately record the characteristics of ambient seawater.

Carbonates have low REY contents, and even a small amount of siliceous debris or other minerals can change its REY abundance and REY pattern (Ling et al., 2013; Hood and Wallace, 2015; Li et al., 2019; Zhao et al., 2021). Based on previous calibrated standards (Th < ~0.5 × 10^{-6} and Th/U < ~0.5, Al < ~100 × 10^{-6}, P$_2$O$_5$ < ~0.03%) (Ling et al., 2013; Hood and Wallace, 2015), four dolomite samples and eight calcite samples were screened. In Fig. 5F, the four dolomites in WR-II Member and WR-III Member all show left-leaning REY patterns (La$_N$/Yb$_N$ = ~0.17–0.46), and all have REY characteristics similar to that of modern seawater (Ce/Ce* ~0.46 ± 0 14; Y/Ho ~ 46.16 ± 9.40). The eight calcite samples all have left-leaning REY patterns (La$_N$/Yb$_N$ = ~0.0016–0.25), the difference is that the LREY of calcites of WR-III Member and UP Member (Ucal) is more depleted (LREY$_N$/HREY$_N$ = ~0.001–0.014, mean ~ 0.007) than the calcites (LREY$_N$/HREY$_N$ = ~0.085–0.122, mean ~ 0.037) of the LP Member (Lcal). Meanwhile, Ucal shows significant negative Ce/Ce* (~0.33 ± 0.45) and high Y/Ho values (~60 ± 15.55) compared to Lcal (~1.38 ± 0.53 and ~ 30.75 ± 5.83, respectively). Low Y/Ho values indicate the implication of terrestrial REY input (Nozaki et al., 1997), and/or possibly anoxic paleoredox conditions (Bau et al., 1997), and Ce enrichment may result from the reductive dissolution of Mn-(oxyhydro) oxide (Wu et al., 2019). Picard et al. (2002) argued that the REY composition of paleo-seawater in the Mesozoic was different from that of modern seawater because the fish and reptile teeth in the carbonate deposits recorded higher Dy$_N$/Yb$_N$ values (>1.8) than in modern seawater (<0.9). In our samples, Lcal (~0.15 ± 0.02) exhibits similar Dy$_N$/Yb$_N$ values with Ucal (~0.14 ± 0.05), indicating that the paleo-seawater in the Doushantuo period was characterized by the HREY enrichment similar to modern seawater. Wu et al. (2019) studied the REY composition of carbonate rocks of the Doushantuo Formation in the Yangtze Gorges area, and most of them show left-leaning REY patterns and super-chondrite Y/Ho values similar to modern seawater. Also, Zhao et al. (2016) reported siliceous rocks from the Doushantuo Formation with modern seawater-like REY composition, which also reflected the chemical composition of ambient seawater during the deposition of siliceous rocks (Murray, 1994). Combined with REY patterns of carbonates in multiple members in this work, it is likely that the REY composition of seawater during the Doushantuo period was very coincident with that of modern seawater and had not been changed significantly.

5.2. REY source of the UP Member

The whole rock REY composition of the UP Member has negative Ce/Ce* and high Y/Ho, similar to modern seawater, but shows MREY enrichment (BSI = ~1.38–1.51) (Table S1, Fig. 5D). The UP Member shows a positive correlation between P$_2$O$_5$ and ΣREY content (R^2 = ~0.40) (Fig. 6A), indicating that REY in UP Member mainly occur in phosphate minerals. These phosphate minerals are apatite, which are considered to be seawater authigenic through mineralogy observation (Fig. 4C and 4D). Low Al$_2$O$_3$ content (~0.08%–0.73%) and weak correlation between ΣREY and Al$_2$O$_3$ of phosphorites (Fig. 6D) are additional indicators. The REY pattern of apatite (UAp-I) is almost consistent with that of modern seawater (Fig. 7A), indicating the main REY source from seawater.

The other type of apatite (UAp-II, Fig. 7A) has the same MREY enrichment as the bulk (Fig. 5D), and has higher ΣREY content than UAp-I. Phosphorites with part of modern seawater characteristics (left-leaning LREY) and MREY enrichment are called "old phosphorites", which is used to describe the Proterozoic-Cambrian phosphorites (Ilyin, 1998). The reason for the MREY enrichment is explained as the heterogeneous REY enrichment during late diagenesis (Reynard et al., 1999), which cause cap-shaped REY patterns. The higher La$_N$/Yb$_N$ or

lower La_N/Sm_N ratios in apatites relative to seawater may indicate that early or late diagenesis occurred (Reynard et al., 1999; Lécuyer et al., 2004; Zhang et al., 2016). In our samples, the apatite in the UP Member has La_N/Yb_N - La_N/Sm_N characteristics close to those of seawater (Fig. 8A), suggesting the minor impact of diagenesis. However, although UAp-II is located in the La_N/Yb_N - La_N/Sm_N characteristic range of seawater, it has enrichment patterns of MREY different from that of modern seawater. A similar REY pattern has also been found in the Ediacaran phosphorites in the middle of Guizhou, which is thought to be related to diagenesis (Yang et al., 2022). UAp-II has higher La_N/Yb_N values than UAp-I with modern seawater characteristics, and the La_N/Yb_N values have a positive correlation with ΣREY ($R^2 = \sim 0.63$, Fig. 8B), indicating that the reason for MREY enrichment may be related to diagenesis. The positive correlation between BSI values and ΣREY also validates diagenetic enrichment (Fig. 8C). In previous works, the early Cambrian apatite with REY enrichment all experienced diagenesis and consisted of numerous nanoscale francolites (Zhang et al., 2022). In contrast, the apatite characterized by structureless aggregates shows a seawater-like REY pattern and has low ΣREY content in the Weng'an phosphorites (Yang et al., 2022). In this study, UAp-II (Fig. 4C) with closely packed francolites may have transformed from UAp-I with irregular aggregates during the diagenesis (Fig. 4D) (Zhang et al., 2022).

The REY in pore water mainly derives from seawater and sediments. Iron (manganese) oxide (hydroxide) and particulate organic carbon in seawater will remove REY into pore water (Haley et al., 2004). Also, the dissolution of clay minerals or heavy minerals in the wall rocks may release a large amount of REY into the pore water (Francovschi et al., 2020). Thus, during diagenesis, apatite can directly capture terrestrial

REY dissolved in pore water, thus having a low Y/Ho value (<44) (Lumiste et al., 2019; Francovschi et al., 2020; Yang et al., 2021). In our samples, the MREY enrichment may be related to terrigenous input because the Y/Ho values show a negative correlation with ΣREY ($R^2 = \sim 0.71$, Fig. 8D). A typical cap-shaped REY pattern is commonly found in the Cambrian phosphorites, which has broader MREY enrichment (from Pr to Ho) than the Ediacaran phosphorites (Zhang et al., 2022). The REY composition of the Ediacaran phosphorites is more similar to that of seawater, and the REY pattern of the francolite is only gradually depleted from Gd to Lu (Yang et al., 2022). Numerous Paleozoic phosphorites (e.g., Cambrian, Silurian, Devonian, Carboniferous) with broad MREY enrichment usually have high ΣREY content, and these REY-enriched phosphorites were considered to record terrigenous REY fluxes (Emsbo et al., 2015; Salama et al., 2018; Lumiste et al., 2021; Yang et al., 2021). The Ediacaran phosphorites with REY enrichment reported by Francovschi et al. (2020) also show an obvious "cap-shaped" REY pattern, and the negative correlation between Y/Ho and REY in the phosphorites indicates that the terrigenous REY input is essential.

5.3. REY source of the LP

The samples with lower P_2O_5 content ($\sim 8.81\% - 14.10\%$) in the LP Member have left-leaning REY patterns (Fig. 5E), which may represent the REY source of seawater. However, the samples with higher P_2O_5 content ($\sim 33.20\% - 38.30\%$) show right-leaning REY patterns, indicating that they have received REY sources other than seawater. Also, the samples with medium P_2O_5 content ($\sim 16.50\% - 23.90\%$) show relatively flat REY patterns, which may be a mixture of different REY
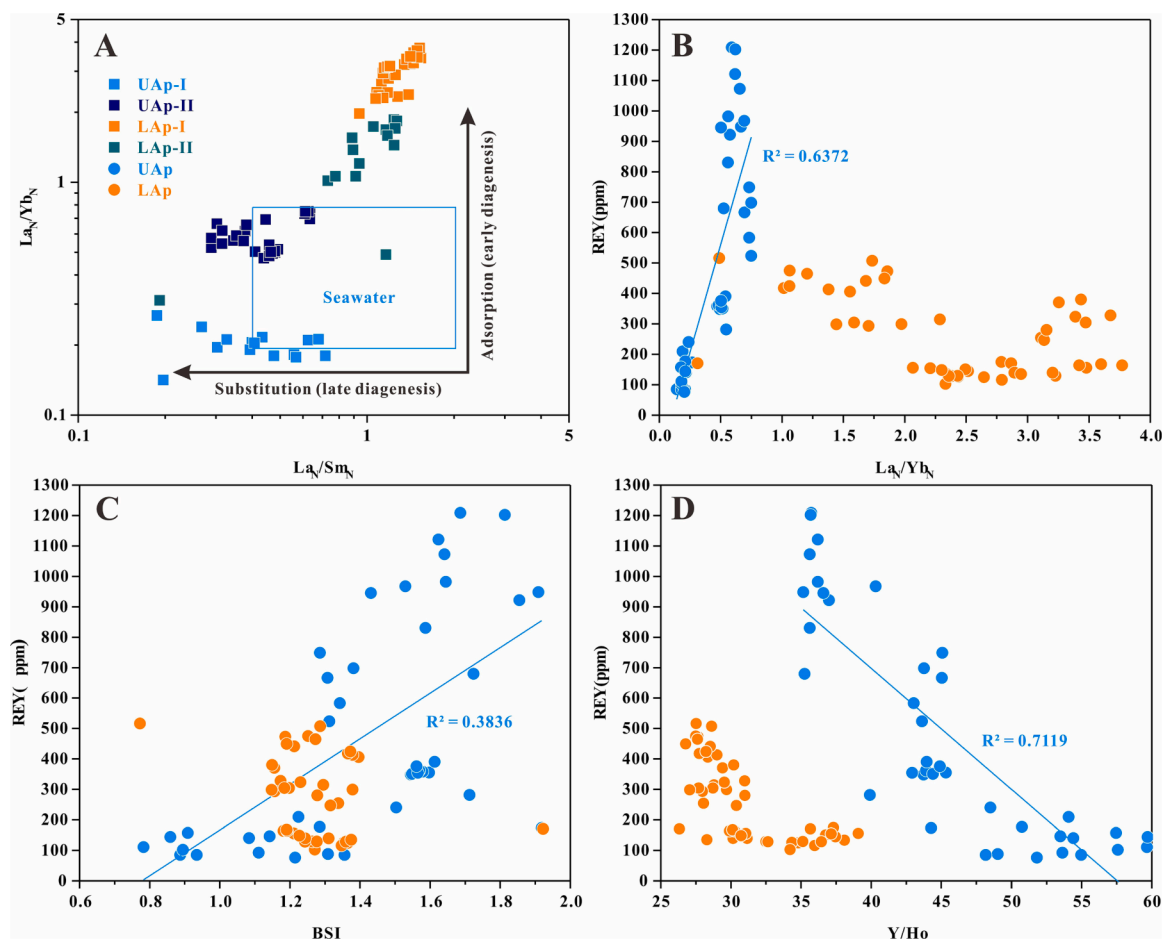
Fig. 8. The La_N/Yb_N values plotted against La_N/Sm_N values of apatites from the upper phosphorite and the lower phosphorite (A). The correlation between ΣREY of La_N/Yb_N (B), BSI (C), and Y/Ho ratios (D) of apatites from the upper phosphorite (UAp) and the lower phosphorite (LAp).

sources. The ΣREY contents of all samples reveal a wide range (51.81–354.39 ppm) and do not correlate with total P_2O_5 concentration (Fig. 6C), indicating that there may be more than one REE source. Through in situ apatite data (Table S2, Fig. 7B), it has been identified that REY patterns in different types of apatites are distinct. The apatite (LAp-I) with a right-leaning REY pattern has a lower ΣREY content (mean ~ 204.08 ppm), while the apatite (LAp-II) with a flat REY pattern has a higher ΣREY content (mean ~ 403.81 ppm). The mineralogical observation is consistent with the in situ apatite REY data and shows two kinds of apatites (Fig. 4G and 4H).

LAp-I with a right-leaning REY pattern shows significantly higher La_N/Yb_N values than modern seawater (Fig. 8A), which may be caused by late diagenesis (Reynard et al., 1999), and LAp-II with a higher ΣREY content than LAp-I may have undergone late diagenesis REY enrichment. However, the La_N/Yb_N value higher than that of seawater does not necessarily indicate diagenesis. For instance, the LREY of most magmatic apatite is usually higher than the HREY (O'Sullivan et al., 2018; Qu et al., 2019). Part of the samples in the LP Member shows significantly higher LREY than HREY, which is completely different from the Ediacaran phosphorites in earlier reports (Yang et al., 2019; Yang et al., 2021). It was suggested that granite commonly shows high LREE compared to HREE, which can be considered as a potential argument (Sha and Chappell, 1999; Pan et al., 2016). Moreover, magmatic apatites usually have a low Sr content and relatively high Mn content, while authigenic apatites have a high Sr content and relatively low Mn content (Hsieh et al., 2008; O'Sullivan et al., 2018; Ansberque et al., 2019). The Sr/Mn values of apatites in LP Member (~2.50–113.18, mean ~ 35.88) are significantly lower than that in UP Member with modern seawater characteristics (~92.68–4801.25, mean 908.68), indicating that the apatite in LP Member may be terrigenous apatite. Meanwhile, the low Y/Ho values of LAp (~26.32–36.44, average ~ 30.02) can also validate the terrigenous input assumption. Moreover, if high ΣREY is caused by the adsorption/substitution of authigenic apatite from massive terrigenous materials during diagenesis, Y/Ho values will have a good correlation with ΣREY (Francovschi et al., 2020). However, there is no such trend in our data (Fig. 8D). Hence, apatites in LP Member may be primarily of terrigenous origin, and their REY characteristics may represent the terrigenous REY composition. Also, LAp-II with flat REY patterns may record mixed REY sources of seawater and terrigenous endmembers, and seawater authigenic apatite in LAp-II can additionally validate it (Fig. 4H).

5.4. Implications

The REY patterns of paleo-seawater have not been well-constrained. As stated earlier, the REY patterns of seawater are consistent with the modern ocean (Shields and Stille, 2001; Shields and Webb, 2004), and this contrasts with the MREY-rich seawater suggested by other groups (Wright et al., 1984; Shaw and Wasserburg, 1985; Grandjean et al., 1987). The Ediacaran phosphorites from the Yangtze Platform have low ΣREY content (~10.09–507.58 ppm) and show modern seawater-like REY patterns (Yang et al., 2021; Yang et al., 2022). Moreover, phosphorites with a modern seawater-like REY pattern are not only distributed in South China but also scattered around other regions of the world (Mazumdar and Banerjee, 1998; Mazumdar et al., 1999; Khan et al., 2016). Apatite (UAp-I) in UP Member and calcite and dolomite in WR-III Member reported in this study have the same REY patterns as modern oxic seawater, possibly indicating the similar REY composition of paleo-seawater to modern seawater as early as the Neoproterozoic period, assuming that the Nanhua Basin had a good connection with the open ocean. In contrast, francolite-like UAp-II does not represent the REY composition of seawater because it may be formed by the transformation of initial amorphous apatite-like UAp-I during diagenesis (Zhang et al., 2022). Moreover, some apatite particles have higher element abundance around the edge than in the center (Lumiste et al., 2019), which is due to element adsorption (especially REY) in pore water by apatite grains

during diagenesis. On a microscale level, an apatite grain with a diameter of hundreds of micrometers may be composed of abundant and different types of nanoscale apatite (e.g., francolite, amorphous apatite, and terrigenous apatite). Thus, a microscale beam spot of LA-ICP-MS may still denude different types of apatites to show mixed trace data. More detailed nanometer-scale investigations are necessary to distinguish different REY and phosphorus sources.

During phosphorite deposition, modern seawater-like REY patterns can be recorded in calcite, dolomite, and apatite. However, the "old phosphorites" shows an MREY-rich pattern, which may result from detrital and/or early/late diagenetic contributions (Reynard et al., 1999; Lumiste et al., 2019; Francovschi et al., 2020; Zhang et al., 2022). In fact, the Ediacaran phosphorites usually contain low ΣREY concentration, the REY enrichment may be mainly derived from the significant terrestrial contribution. For instance, Francovschi et al. (2020) reported the REY-rich phosphorites from the late Ediacaran Kalyus Beds and suggested the importance of terrestrial contribution accompanied by accumulation of REY by apatite during late diagenesis. This could be very similar to the observations in the Nanhua Basin where the near-shore phosphorites (Kaiyang, ~114–423 ppm; Fangmashan, ~52–357 ppm) commonly show higher REY than the off-shore phosphorites (Weng'an, ~19–258 ppm) (Xiao et al., 2018; Yang et al., 2019). Also, the ΣREY concentration of terrigenous material is a critical factor in affecting the ΣREY content of phosphorites. The ΣREY content of the Doushantuo phosphorites is found to be low, which may be explained by the low ΣREY concentration of terrigenous input. Meanwhile, the late Ediacaran phosphorites from the Kalyus Beds are REY-enriched because basalts and granites weathering support massive REY (Francovschi et al., 2020). The REY enrichment of the Cambrian phosphorites from the southern prospects in the Georgina basin of Australia is explained by the surface and groundwater interaction with A-type granites and schistose metasedimentary basement rocks (Matthew et al., 2022), thus the REY enrichment in phosphorites can be mainly related to the REY-enriched igneous rocks. As a result, not only is it possible that the abundance of REY in phosphorite deposits is a result of weathering of terrigenous rocks, but also the basement rocks that have undergone weathering have high concentrations of REY.

6. Conclusions

In this study, phosphorites, in situ apatite, and carbonate minerals from the Doushantuo Formation in South China were investigated by applying mineralogy, bulk-geochemistry, and in situ geochemistry to understand the REY composition of paleo-seawater and terrigenous endmembers. The obtained results indicate that the Doushantuo seawater was characterized by a REY-PAAS pattern with HREE enrichment similar to modern seawater, and the terrigenous endmember may show an HREY-depleted REY-PAAS pattern. Although the UP Member received terrigenous REY input during early diagenesis, the REY of the UP Member is mainly derived from the seawater column. The REY of LP Member is dominated by the terrigenous endmember and is slightly affected by seawater REY. Combined with previous works, the ΣREY concentration of Doushantuo seawater is very low, which cannot result in REY enrichment in phosphorites unless it was mixed with other REY-enriched sources.

Declaration of Competing Interest

The authors declare that they have no known competing financial interests or personal relationships that could have appeared to influence the work reported in this paper.

Data availability

Our data is included in the supplementary materials.

Acknowledgements

Appendix A. Supplementary data

Supplementary data to this article can be found online at https://doi.org/10.1016/j.oregeorev.2023.105470.

References

Alibo, D.S., Nozaki, Y., 1999. Rare earth elements in seawater: particle association, shale-normalization, and Ce oxidation. Geochim. Cosmochim. Acta. 63 (3), 363–372.

Ansberque, C., Mark, C., Caulfield, J.T., Chew, D.M., 2019. Combined in-situ determination of halogen (F, Cl) content in igneous and detrital apatite by SEM-EDS and LA-Q-ICPMS: A potential new provenance tool. Chem. Geol. 524, 406–420.

Baioumy, H., Farouk, S., 2022. The geochemical and economic significance of REE in the Upper Cretaceous-Eocene Tethyan phosphorites. J. Afr. Earth. Sci. 194, 104635.

Bau, M., 1991. Rare-earth element mobility during hydrothermal and metamorphic fluid-rock interaction and the significance of the oxidation state of europium. Chem. Geol. 93 (3), 219–230.

Bau, M., Dulski, P., 1996. Distribution of yttrium and rare-earth elements in the Penge and Kuruman iron-formations, Transvaal Supergroup. South Africa. Precambrian Res. 79 (1), 37–55.

Bau, M., Möller, P., Dulski, P., 1997. Yttrium and lanthanides in eastern Mediterranean seawater and their fractionation during redox-cycling. Mar. Chem. 56 (1), 123–131.

Chen, M.Z., Fu, Y., Xia, Y., Xie, Z.J., Zhou, K.L., Zhang, P., 2019. A prospective analysis on REE resources of the phosphorite-type REE ore deposits in. China Acta Mineralogica Sinica. 39 (4), 345–358 in Chinese with English abstract.

Condon, D., Zhu, M., Bowring, S., Wang, W., Yang, A., Jin, Y., 2005. U-Pb Ages from the Neoproterozoic Doushantuo Formation. China. Science. 308 (5718), 95–98.

Cook, P.J., Shergold, J.H., 1984. Phosphorus, phosphorites and skeletal evolution at the Precambrian—Cambrian boundary. Nature. 308 (5956), 231–236.

Elderfield, H., Hawkesworth, C.J., Greaves, M.J., Calvert, S.E., 1981. Rare earth element geochemistry of oceanic ferromanganese nodules and associated sediments. Geochim. Cosmochim. Acta. 45 (4), 513–528.

Emsbo, P., McLaughlin, P.I., Breit, G.N., du Bray, E.A., Koenig, A.E., 2015. Rare earth elements in sedimentary phosphate deposits: Solution to the global REE crisis? Gondwana Res. 27 (2), 776–785.

Francovschi, I., Grädinaru, E., Roban, R.-D., Ducea, M.N., Ciobotaru, V., Shumlyanskyy, L., 2020. Rare earth element (REE) enrichment of the late Ediacaran Kalyus Beds (East European Platform) through diagenetic uptake. Geochemistry. 80 (2), 125612.

Gao, L.Z., Zhang, H., Zhang, C.H., Ding, X.Z., Yin, C.Y., Wu, Z.J., Song, B., 2018. Collate and Stipulate the Sequences of the Mesoproterozoic Kunyang Group in Eastern Yunnan and Its Position inStratigraphic Column of China. Geological Review. 64 (02), 283–298 in Chinese with English abstract.

Gong, Q., Li, F., Lu, C., Wang, H., Tang, H., 2021. Tracing seawater- and terrestrial-sourced REE signatures in detritally contaminated, diagenetically altered carbonate rocks. Chem. Geol. 570, 120169.

Grandjean, P., Cappetta, H., Michard, A., Albare'de, F., 1987. The assessment of REE patterns and 143Nd/144Nd ratios in fish remains. Earth Planet. Sci. Lett. 84(2):181-196.

Grandjean-Lécuyer, P., Feist, R., Albarède, F., 1993. Rare earth elements in old biogenic apatites. Geochim. Cosmochim. Acta. 57 (11), 2507–2514.

Haley, B.A., Klinkhammer, G.P., McManus, J., 2004. Rare earth elements in pore waters of marine sediments. Geochim. Cosmochim. Acta. 68 (6), 1265–1279.

Hoffman, P.F., Abbot, D.S., Ashkenazy, Y., Benn, D.I., Brocks, J.J., Cohen, P.A., Cox, G. M., Creveling, J.R., Donnadieu, Y., Erwin, D.H., Fairchild, I.J., Ferreira, D., Goodman, J.C., Halverson, G.P., Jansen, M.F., Le Hir, G., Love, G.D., Macdonald, F. A., Maloof, A.C., Partin, C.A., Ramstein, G., Rose, B.E.J., Rose, C.V., Sadler, P.M., Tziperman, E., Voigt, A., Warren, S.G., 2017. Snowball Earth climate dynamics and Cryogenian geology-geobiology. Science Advances. 3 (11), e1600983.

Hood, A.V.S., Wallace, M.W., 2015. Extreme ocean anoxia during the Late Cryogenian recorded in reefal carbonates of Southern Australia. Precambrian Res. 261, 96–111.

Hsieh, P.S., Chen, C.H., Yang, H.J., Lee, C.Y., 2008. Petrogenesis of the Nanling Mountains granites from South China: Constraints from systematic apatite geochemistry and whole-rock geochemical and Sr–Nd isotope compositions. J. Asian Earth Sci. 33 (5), 428–451.

Ilyin, A.V., 1998. Rare-earth geochemistry of 'old' phosphorites and probability of syngenetic precipitation and accumulation of phosphate1In memory of Richard P. Sheldon1. Chem. Geol. 144 (3), 243–256.

Jiang, G.Q., Shi, X.Y., Zhang, S.H., Wang, Y., Xiao, S.H., 2011. Stratigraphy and paleogeography of the Ediacaran Doushantuo Formation (ca. 635–551Ma) in South China. Gondwana Res. 19 (4), 831–849.

Kennedy, M.J., Runnegar, B., Prave, A.R., Hoffmann, K.H., Arthur, M.A., 1998. Two or four Neoproterozoic glaciations? Geology. 26 (12), 1059–1063.

Khan, K.F., Dar, S.A., Khan, S.A., 2012. Rare earth element (REE) geochemistry of phosphorites of the Sonrai area of Paleoproterozoic Bijawar basin, Uttar Pradesh. India. Journal of Rare Earths. 30 (5), 507–514.

Khan, S.A., Khan, K.F., Dar, S.A., 2016. REE geochemistry of Early Cambrian phosphorites of Masrana and Kimoi blocks, Uttarakhand. India. Arabian J. Geosci. 9 (6), 456.

Khelalfa, A., Delimi, R., Benredjem, Z., 2016. Distribution and extraction of chromium from phosphate ore. J. Water Reuse Desalin. 6 (4), 524–532.

Lécuyer, C., Reynard, B., Grandjean, P., 2004. Rare earth element evolution of Phanerozoic seawater recorded in biogenic apatites. Chem. Geol. 204 (1), 63–102.

Li, X.H., 1999. U-Pb zircon ages of granites from the southern margin of the Yangtze Block: timing of Neoproterozoic Jinning: Orogeny in SE China and implications for Rodinia Assembly. Precambrian Res. 97 (1), 43–57.

Li, C., Love, G.D., Lyons, T.W., Fike, D.A., Sessions, A.L., Chu, X., 2010. A stratified redox model for the Ediacaran Ocean. Science. 328 (5974), 80–83.

Li, F., Webb, G.E., Algeo, T.J., Kershaw, S., Lu, C.J., Oehlert, A.M., Gong, Q.L., Pourmand, A., Tan, X.C., 2019. Modern carbonate ooids preserve ambient aqueous REE signatures. Chem. Geol. 509, 163–177.

Li, C., Zhu, M., Feng, Q., Clausen, S., 2021. Editorial: The co-evolution of life and environments in South China from Snowball Earth to Cambrian Explosion. Palaeogeogr. Palaeoclimatol. Palaeoecol. 563, 110181.

Liang, C.M., 1984. Sedimentary framework of the late Sinian Doushantuo period in western hubei and its control of phosphate deposit. Journal of. Jilin University (Earth Science Edition). (03):46–57 in Chinese with English abstract.

Ling, H.F., Chen, X., Li, D., Wang, D., Shields-Zhou, G.A., Zhu, M.Y., 2013. Cerium anomaly variations in Ediacaran–earliest Cambrian carbonates from the Yangtze Gorges area, South China: Implications for oxygenation of coeval shallow seawater. Precambrian Res. 225, 110–127.

Liu, Y.S., Hu, Z.C., Gao, S., Günther, D., Xu, J., Gao, C.G., Chen, H.H., 2008. In situ analysis of major and trace elements of anhydrous minerals by LA-ICP-MS without applying an internal standard. Chem. Geol. 257 (1), 34–43.

Liu, X.-M., Kah, L.C., Knoll, A.H., Cui, H., Wang, C., Bekker, A., Hazen, R.M., 2021. A persistently low level of atmospheric oxygen in Earth's middle age. Nat. Commun. 12 (1).

Liu, Q.Y., 2012. Composition and element geochemistry of Fangmashan, Hubei province. Geology Of Chemical Minerals. 34(4):9 in Chinese with English abstract.

Lumiste, K., Mänd, K., Bailey, J., Paiste, P., Lang, L., Lepland, A., Kirsimäe, K., 2019. REE +Y uptake and diagenesis in Recent sedimentary apatites. Chem. Geol. 525, 268–281.

Lumiste, K., Lang, L., Paiste, P., Lepland, A., Kirsimäe, K., 2021. Heterogeneous REE+Y distribution in Early Paleozoic shelly phosphorites: Implications for enrichment mechanisms. Chem. Geol. 586, 120590.

Luo, D.K., 2011. Research on geochemistry characteristics and cause of formation of Jingxiang phosphorus deposit in Hubei, China. (Ph. D Thesis), China University of Geosciences (Beijing), 66 pp (in Chinese with English abstract).

Matthew, V., Diana, Z., Carl, S., Helen, D., Micaela, G., 2022. REE enrichment of phosphorites: An example of the Cambrian Georgina Basin of Australia. Chem. Geol. 588, 120654.

Mazumdar, A., Banerjee, D.M., 1998. Siliceous sponge spicules in the Early Cambrian chert-phosphorite member of the Lower Tal Formation, Krol belt. Lesser Himalaya. Geology. 26 (10), 899–902.

Mazumdar, A., Banerjee, D.M., Schidlowski, M., Balaram, V., 1999. Rare-earth elements and Stable Isotope Geochemistry of early Cambrian chert-phosphorite assemblages from the Lower Tal Formation of the Krol Belt (Lesser Himalaya, India). Chem. Geol. 156 (1), 275–297.

McArthur, J.M., Walsh, J.N., 1984. Rare-earth geochemistry of phosphorites. Chem. Geol. 47 (3), 191–220.

Mi, W.T., 2010. The sequence stratigraphy and genesis of phosphorites of doushantuo formation at Baiguoyuan, Yichang. Hubei. Acta Sedimentol. Sinica. 28 (3), 471–480 in Chinese with English abstract.

Murray, R.W., 1994. Chemical criteria to identify the depositional environment of chert: general principles and applications. Sediment. Geol. 90 (3), 213–232.

Nozaki, Y., 2001. Rare Earth Elements and their Isotopes in the Ocean. In: Steele, J.H. (Ed.), Encyclopedia of Ocean Sciences. Academic Press, Oxford, pp. 2354–2366.

Nozaki, Y., Zhang, J., Amakawa, H., 1997. The fractionation between Y and Ho in the marine environment. Earth Planet. Sci. Lett. 148 (1), 329–340.

O'Sullivan, G.J., Chew, D.M., Morton, A.C., Mark, C., Henrichs, I.A., 2018. An Integrated Apatite Geochronology and Geochemistry Tool for Sedimentary Provenance Analysis. Geochem. Geophys. Geosyst. 19 (4), 1309–1326.

Pan, L.C., Hu, R.Z., Wang, X.S., Bi, X.W., Zhu, J.J., Li, C.S., 2016. Apatite trace element and halogen compositions as petrogenetic-metallogenic indicators: Examples from four granite plutons in the Sanjiang region, SW China. Lithos. 254–255, 118–130.

Picard, S., Lécuyer, C., Barrat, J.A., Garcia, J.P., Dromart, G., Sheppard, S.M.F., 2002. Rare earth element contents of Jurassic fish and reptile teeth and their potential relation to seawater composition (Anglo-Paris Basin, France and England). Chem. Geol. 186 (1), 1–16.

Piper, D.Z., 1974. Rare earth elements in the sedimentary cycle: A summary. Chem. Geol. 14 (4), 285–304.

Pufahl, P.K., Groat, L.A., 2017. Sedimentary and Igneous Phosphate Deposits: Formation and Exploration: An Invited Paper. Economic Geology. 112 (3), 483–516.

Qu, P., Li, N.-B., Niu, H.-C., Yang, W.-B., Shan, Q., Zhang, Z.-Y., 2019. Zircon and apatite as tools to monitor the evolution of fractionated I-type granites from the central Great Xing'an Range. NE China. Lithos. 348-349, 105207.

Reinhard, C.T., Planavsky, N.J., Gill, B.C., Ozaki, K., Robbins, L.J., Lyons, T.W., Fischer, W.W., Wang, C., Cole, D.B., Konhauser, K.O., 2017. Evolution of the global phosphorus cycle. Nature. 541 (7637), 386–389.

Reynard, B., Lécuyer, C., Grandjean, P., 1999. Crystal-chemical controls on rare-earth element concentrations in fossil biogenic apatites and implications for paleoenvironmental reconstructions. Chem. Geol. 155 (3), 233–241.

Sahoo, S.K., Planavsky, N.J., Kendall, B., Wang, X., Shi, X., Scott, C., Anbar, A.D., Lyons, T.W., Jiang, G., 2012. Ocean oxygenation in the wake of the Marinoan glaciation. Nature. 489 (7417), 546–549.

Salama, W., Khirekesh, Z., Amini, A., Bafti, B.S., 2018. Diagenetic evolution of the upper Devonian phosphorites, Alborz Mountain Range, northern Iran. Sediment. Geol. 376, 90–112.

Sha, L., Chappell, B.W., 1999. Apatite chemical composition, determined by electron microprobe and laser-ablation inductively coupled plasma mass spectrometry, as a probe into granite petrogenesis. Geochim. Cosmochim. Acta. 63 (22), 3861–3881.

Shaw, H.F., Wasserburg, G.J., 1985. Sm-Nd in marine carbonates and phosphates: Implications for Nd isotopes in seawater and crustal ages. Geochim. Cosmochim. Acta. 49 (2), 503–518.

Shields, G., Stille, P., 2001. Diagenetic constraints on the use of cerium anomalies as palaeoseawater redox proxies: an isotopic and REE study of Cambrian phosphorites. Chem. Geol. 175 (1), 29–48.

Shields, G.A., Webb, G.E., 2004. Has the REE composition of seawater changed over geological time? Chem. Geol. 204 (1), 103–107.

Sholkovitz, E.R., Landing, W.M., Lewis, B.L., 1994. Ocean particle chemistry: The fractionation of rare earth elements between suspended particles and seawater. Geochim. Cosmochim. Acta. 58 (6), 1567–1579.

Taylor, S.R., McLennan, S.M., 1985. The Continental Crust: its Composition and Evolution. In: An Examination of the Geochemical Record Preserved in Sedimentary Rocks. Blackwell Scientific Publications, Oxford, p. 312.

Tian, S.P., 2000. Typical features and distribution of Chinese phosphorite deposits. Geology of chemical minerals. (01):11-16 in Chinese with English abstract.

Toyoda, K., Nakamura, Y., Masuda, A., 1990. Rare earth elements of Pacific pelagic sediments. Geochim. Cosmochim. Acta. 54 (4), 1093–1103.

Vernhet, E., 2007. Paleobathymetric influence on the development of the late Ediacaran Yangtze platform (Hubei, Hunan, and Guizhou provinces, China). Sediment. Geol. 197 (1), 29–46.

Wright, J., Seymour, R.S., Shaw, H.F., Clark, D.L., 1984. REE and Nd isotopes in conodont apatite: Variations with geological age and depositional environment. Special Paper of the Geological Society of America. 196, 325–340.

Wright, J., Schrader, H., Holser, W.T., 1987. Paleoredox variations in ancient oceans recorded by rare earth elements in fossil apatite. Geochim. Cosmochim. Acta. 51 (3), 631–644.

Wu, H.P., Jiang, S.Y., Palmer, M.R., Wei, H.Z., Yang, J.H., 2019. Positive cerium anomaly in the Doushantuo cap carbonates from the Yangtze platform, South China: Implications for intermediate water column manganous conditions in the aftermath of the Marinoan glaciation. Precambrian Res. 320, 93–110.

Xiao, C.Y., Zhang, Z.W., He, C.Z., Wen, H.J., Fan, H.F., 2018. The Depositional Environment of Ediacaran Phosphorite Deposits, South China. Bulletin of Mineralogy, Petrology and Geochemistry. 37 (1), 121–138 in Chinese with English abstract.

Xin, H., Jiang, S.Y., Yang, J.H., Wu, H.P., Pi, D.H., 2015. Rare earth element and Sr–Nd isotope geochemistry of phosphatic rocks in Neoproterozoic Ediacaran Doushantuo Formation in Zhangcunping section from western Hubei Province, South China. Palaeogeogr. Palaeoclimatol. Palaeoecol. 440, 712–724.

Xiong, X.X., Xue, T.X., Chai, J.H., Niu, G.Z., 2010. Geologic and resource perspectives analysis of phosphorite concentrated district in western Hubei province. Geology of chemical minerals. 32(01):1-18 in Chinese with English abstract.

Xu, D., Wang, X., Zhu, J.M., Jiang, G., Shi, X., Wang, X., Sahoo, S.K., 2022. Chromium isotope evidence for oxygenation events in the Ediacaran Ocean. Geochim. Cosmochim. Acta. 323, 258–275.

Yang, H., Xiao, J., Xia, Y., Xie, Z., Tan, Q., Xu, J., Guo, H., He, S., Wu, S., 2019. Origin of the Ediacaran Weng'an and Kaiyang phosphorite deposits in the Nanhua basin. SW China. J. Asian Earth Sci. 182, 103931.

Yang, H., Xiao, J., Xia, Y., Xie, Z., Tan, Q., Xu, J., He, S., Wu, S., Liu, X., Gong, X., 2021. Phosphorite generative processes around the Precambrian-Cambrian boundary in South China: An integrated study of Mo and phosphate O isotopic compositions. Geosci. Front. 12 (5), 101187.

Yang, H.Y., Xiao, J.F., Xia, Y., Zhao, Z.F., Xie, Z.J., He, S., Wu, S.W., 2022. Diagenesis of Ediacaran−early Cambrian phosphorite: Comparisons with recent phosphate sediments based on LA-ICP-MS and EMPA. Ore Geol. Rev. 144, 104813.

Zhang, L., Algeo, T.J., Cao, L., Zhao, L.S., Chen, Z.Q., Li, Z.H., 2016. Diagenetic uptake of rare earth elements by conodont apatite. Palaeogeography, Palaeoclimatology, Palaeoecology. 458, 176–197.

Zhang, H.J., Fan, H.F., Wen, H.J., Han, T., Zhou, T., Xia, Y., 2022. Controls of REY enrichment in the early Cambrian phosphorites. Geochim. Cosmochim. Acta. 324, 117–139.

Zhao, Y.Y., Jiang, S.Y., Li, D., Yang, J.H., 2016. A petrographic and geochemical study of carbonate and silica phases from the Ediacaran Doushantuo Formation in the Three Gorges area of South China: Implications for diagenetic conditions. Palaeogeogr. Palaeoclimatol. Palaeoecol. 463, 150–167.

Zhao, Y.Y., Wei, W., Li, S.Z., Yang, T., Zhang, R.X., Somerville, I., Santosh, M., Wei, H.T., Wu, J.Q., Yang, J., Chen, W., Tang, Z.N., 2021. Rare earth element geochemistry of carbonates as a proxy for deep-time environmental reconstruction. Palaeogeogr. Palaeoclimatol. Palaeoecol. 574, 110443.

Zhao, M.Y., Zheng, Y.F., 2014. Marine carbonate records of terrigenous input into Paleotethyan seawater: Geochemical constraints from Carboniferous limestones. Geochim. Cosmochim. Acta. 141, 508–531.

Zhu, M.Y., Lu, M., Zhang, J.M., Zhao, F.C., Li, G.X., Aihua, Y., Zhao, X., Zhao, M.J., 2013. Carbon isotope chemostratigraphy and sedimentary facies evolution of the Ediacaran Doushantuo Formation in western Hubei. South China. Precambrian Res. 225, 7–28.